Title

Evaluation of affine fiber kinematics in porcine tricuspid valve leaflets using polarized spatial frequency domain imaging and planar biaxial testing.

Authors

Ross, Colton

Mullins, Brennan

Hillshafer, Clare

et al.

Publication Date

2021-06-23

DOI

10.1016/j.jbiomech.2021.110475

Peer reviewed

Published in final edited form as:
J Biomech. 2021 June 23; 123: 110475. doi:10.1016/j.jbiomech.2021.110475.

Evaluation of affine fiber kinematics in porcine tricuspid valve leaflets using polarized spatial frequency domain imaging and planar biaxial testing

Colton J. Ross[a], **Brennan T. Mullins**[a], **Clare E. Hillshafer**[a], **Arshid Mir**[b], **Harold M. Burkhart**[c], **Chung-Hao Lee**[a,d,*]

[a]Biomechanics and Biomaterials Design Laboratory (BBDL), School of Aerospace and Mechanical Engineering, University of Oklahoma, Norman, USA

[b]Department of Pediatrics

[c]Department of Surgery, University of Oklahoma Health Sciences Center (OUHSC), Oklahoma City, USA

[d]Institute for Biomedical Engineering, Science and Technology, University of Oklahoma, Norman, USA

Abstract

Collagen fibers are the primary load-bearing microstructural constituent of bodily soft tissues, and, when subjected to external loading, the collagen fibers reorient, uncrimp, and elongate. Specific to the atrioventricular heart valve leaflets, the collagen fiber kinematics form the basis of many constitutive models; however, some researchers claim that modeling the affine fiber kinematics (AFK) are sufficient for accurately predicting the macroscopic tissue deformations, while others state that modeling the non-affine kinematics (i.e., fiber uncrimping together with elastic elongation) is required. Experimental verification of the AFK theory has been previously performed for the mitral valve leaflets in the left-side heart; however, this same evaluation has yet to be performed for the morphologically distinct tricuspid valve (TV) leaflets in the right-side heart. In this work, we, *for the first time*, evaluated the AFK theory for the TV leaflets using an integrated biaxial testing-polarized spatial frequency domain imaging device to experimentally quantify the load-dependent collagen fiber reorientations for comparison to the AFK theory predictions. We found that the AFK theory generally underpredicted the fiber reorientations by 3.1°, on average, under the applied equibiaxial loading with greater disparity when the tissue was subjected to the applied non-equibiaxial loading. Furthermore, increased AFK errors were observed with increasing collagen fiber reorientations (Pearson coefficient $r = -0.36$, equibiaxial loading), suggesting the AFK theory is better suited for relatively smaller reorientations. Our findings suggest the AFK theory may require modification for more accurate predictions of the collagen fiber kinematics in the TV leaflets, which will be useful in refining modeling efforts for more accurate TV simulations.

*Corresponding author. 865 Asp Ave., Felgar Hall 219C, Norman, OK 73019, USA. ch.lee@ou.edu (Chung-Hao Lee).

Conflict of Interest. The authors of this paper have no financial or personal relationships with other people or organizations that could inappropriately influence (bias) our work.

Keywords

heart valves; collagen fibers; polarized light collagen imaging; soft tissue biomechanics; collagen reorientations

1. Introduction

The mechanical behaviors and material anisotropy of soft tissues are connected to the underlying microstructure, which consists of collagen fibers embedded in a nonfibrous matrix. Constitutive models based on hyperelasticity theory enable modeling of the behaviors of the microstructural components and connecting those microscopic, microstructural, and mechanical contributions to the macroscopic material deformations. Using this approach, constitutive formulation becomes straightforward by including the mechanics of the collagen fibers, elastin fibers, and nonfibrous matrix; however, the proper assumptions for modeling the microstructural contributions, such as the collagen or elastin fiber kinematics and the fiber and nonfibrous matrix coupling, have yet to be systematically determined for some tissues, such as the atrioventricular heart valve (AHV) leaflets. The collagen fibers in the AHV leaflets are naturally crimped with a preferential alignment to the circumferential tissue direction (Kunzelman et al., 1993; Sacks and Yoganathan, 2007). As loading is applied to the tissue, the collagen fibers reorient towards the primary loading direction, which contributes to the low-stress “toe-region” of the stress-stretch behaviors. After reorientation, the fibers uncrimp and elongate, which manifests as the high-stress, asymptotic regime. The collagen fiber kinematics form the basis of many constitutive models, but there remains no consensus on how the collagen model should be formulated: some AHV leaflet models are based on affine fiber kinematics (AFK) (Anssari-Benam and Bucchi, 2018; Jacobs et al., 2013; Lanir, 2017; Lee et al., 2015; Fan and Sacks, 2014), while other models include the non-affine fiber kinematics (non-AFK), especially when tissue viscoelasticity is critical (Bianchi et al., 2020; Dhume and Barocas, 2019; Morin et al., 2018). Herein, AFK is defined as a homogeneous deformation in which the fibers, usually considered as straight fibers without crimp, follow the tissue-level specimen deformation (e.g., parallel fibers in the reference configuration map to parallel fibers in the deformed configuration) (Tadmor et al., 2012). On the other hand, non-AFK is characterized by fibers undergoing inhomogeneous deformations that do not follow the macroscopic tissue deformation, potentially caused by shear deformations or fiber elongation and uncrimping.

Previous studies on soft tissue biomechanics have shown that the use of the AFK theory must be validated on a per-tissue basis. This is exemplified by the finding of a prior study that a modified AFK theory is required for the mitral valve (MV) leaflets (Lee et al., 2015), while other studies of tendons or small intestinal submucosa have noted the AFK theory to be invalid, especially in cases of large strain (Jayyosi et al., 2017; Lake et al., 2012a; Billiar and Sacks, 1997; Gilbert et al., 2006). Moreover, some researchers have noted the *in vitro* tissue testing conditions could affect the observed fiber kinematics. For example, some studies of soft tissues, such as liver, skin, and arteries, conducted bulge/inflation testing and noted minimal fiber reorientations (Cavinato et al., 2017; Jayyosi et al., 2017), while other studies have performed uniaxial testing of tendons and observed significant fiber

reorientations and non-AFK behaviors (Cavinato et al., 2020; Jayyosi et al., 2017; Lake et al., 2012a). It has also been suggested that interactions between collagen fibers and the nonfibrous matrix could play a role in the accuracy of the AFK assumption. Specifically, a stiffer nonfibrous matrix could result in more non-AFK behaviors as the fibers cannot easily reorient (Zhang et al., 2013). Those observations and theories from previous studies necessitate additional examinations of the AFK theory and further insight to the collagen fiber architecture (CFA) of specific tissues, such as the tricuspid valve (TV) leaflets. While a prior study has been performed to evaluate the AFK of the MV leaflets (Lee et al., 2015), the TV leaflets undergo a lower pressure gradient in the right side of the heart compared to their MV counterpart on the left side of the heart, i.e., 25 mmHg vs. 100 mmHg (Khoiy and Amini, 2016; Pierlot et al., 2015). Thus, these AHV tissues that have different functional environments may have different microstructural properties and behaviors that necessitate their own AFK-based investigations (Jett et al., 2018; Kramer et al., 2019).

In this work, we provide a *first-of-its-kind* evaluation of the AFK assumption for the tricuspid valve leaflets using an integrated biaxial testing-polarized spatial frequency domain imaging (pSFDI) device. The non-destructive collagen fiber imaging technique enabled quantification of the load-dependent changes in the CFA of the TV leaflets, which were then compared to the predictions of the AFK theory to evaluate the viability in capturing the collagen fiber reorientations. Unlike previous studies using small-angle light scattering (Sacks et al., 1997, 1998), our approach is beneficial as the pSFDI modality does not require tissue fixation, allowing for the observation of collagen fiber reorientations and fiber kinematics within the same tissue specimen. Additionally, the biaxial testing scheme was rarely performed in the previous AFK-based experiments for the mitral valve leaflets and the other tissues (Lee et al., 2015; Pham et al., 2017), and thus, our findings could be helpful for understanding differences in collagen fiber kinematics under different experimental testing conditions. The results of this work will be useful for a refined understanding of AFK in the TV leaflets and for future refinement of accurate microstructure-informed constitutive models and TV simulations.

2. Methods

2.1. Tissue acquisition and preparation

Porcine hearts were obtained from Animal Technologies (Dallas, TX) and stored in a freezer at −14 °C for prolonged tissue storage. Freezer storage of the tissues was performed based on our previous work that demonstrated minimal changes in the observed mechanical properties between the fresh (unfrozen) and frozen tissues (Duginski et al., 2020). At the time of testing, the hearts were thawed, and the tricuspid valves were dissected (Fig. 1a) to retrieve the TV anterior leaflets, posterior leaflets, and septal leaflets (TVAL, $n = 11$; TVPL, $n = 14$; TVSL, $n = 12$). After dissection, the leaflets were further sectioned to obtain a 10×10 mm specimen from the central, belly region of the leaflet (Fig. 1b). The square specimens were then mounted to a commercial biaxial testing device (CellScale, Canada) via tined BioRakes (Fig. 1c), with the tissue's circumferential (Circ) and radial (Rad) directions aligned with the X- and Y-directions of the BioTester, respectively. The biaxial testing device was further equipped with an in-house pSFDI device (Fig. 1d), which was used in the

quantification of the CFAs of the TV leaflet specimens (see Section 2.3). Once the tissues were mounted to the biaxial testing system, glass beads were used to construct a 2×2 fiducial marker array in the center of the specimen for later tissue strain calculation based on digital image correlation (Jett et al., 2018; Ross et al., 2019). Tissues were then submerged in a 32 °C phosphate-buffered saline bath to emulate the physiological temperature. A temperature level slightly lower than body temperature (37 °C) was used to avoid previously observed issues related to polarizer fogging in the pSFDI portion of the experiment (Jett et al., 2020; Hudson et al., 2020).

2.2. Biaxial mechanical testing

Biaxial mechanical testing was performed following our established protocols (Jett et al., 2018; Laurence et al., 2019). First, tissues were preconditioned through ten equibiaxial loading/unloading cycles to a targeted membrane tension of 50 N/m to emulate the physiologic loading of the valve leaflets (Khoiy and Amini, 2016). After preconditioning, tissue specimens were then biaxially loaded with varying ratios of biaxial tensions: $T_{Circ}:T_{Rad} = 1:1, 0.66:1, 0.33:1, 1:0.66$, and 1:0.33 (Fig. 1e). Each loading ratio was repeated for 4 loading/unloading cycles to ensure repeatability of the stress-strain behaviors, and the final loading cycle was used for tissue stress-stretch analysis. Throughout testing, the load cell readings were recorded and images were captured by a CCD camera at 5 Hz. After biaxial testing was completed, the pSFDI component of the integrated instrument was used to quantify the load-dependent CFAs of the TV leaflet specimens (Hudson et al., 2020; Jett et al., 2020).

2.3. Quantification of the load-dependent changes in collagen fiber architecture

To quantify the changes in the load-dependent CFA, an in-house pSFDI device was used (Fig. 1d). This device has been used in previous works from our laboratory, and the reader is referred to the pSFDI theory and details about the experimental procedure (Hudson et al., 2020; Jett et al., 2020). Briefly, the imaging modality relies on the polarization-dependent diattenuating properties of collagen fibers to quantify the collagen fiber orientations. The imaging sequence contains:

- a digital light projector casting incident light through a polarizer and onto the specimen at an angle $\theta_{polarizer}$.
- the polarized light reflected off of the specimen with an intensity I.
- the reflected light passing back through the polarizer at the angle $\theta_{polarizer}$ and an image captured by a CCD camera.

The sequence is repeated for $\theta_{polarizer} = 0^{\circ} - 180^{\circ}$ at 5° increments. Then, the light intensity-$\theta_{polarizer}$ response of the tissue was fit with a three-term Fourier series,

$$I = \gamma_0 + \gamma_2[2(\theta_{fiber} - \theta_{polarizer}) + \gamma_4[4(\theta_{fiber} - \theta_{polarizer})], \quad (1)$$

where γ_0 represents the mean light intensity, and γ_2 and γ_4 are the coefficients representing the optical anisotropy. The experimentally measured fiber angle θ_{fiber} was determined as the $\theta_{polarizer}$ corresponding to the peak reflected light intensity I. Furthermore, the determined Fourier coefficients were then used to quantify the degree of optical anisotropy (DOA):

$$\mathrm{DOA} = \frac{\gamma_2 + \gamma_4}{\gamma_0 + \gamma_2 + \gamma_4}. \tag{2}$$

The DOA is an optically based metric that describes the level of preferential fiber alignment along θ_{fiber}. Note that θ_{fiber} and the DOA were calculated on a pixel-by-pixel basis, offering a detailed representation of the spatially varying CFA of the TV leaflets. The pSFDI sequence was repeated at the post-preconditioning (PPC) configuration and at the deformation associated with the peak loading of each biaxial tension protocol to obtain the fiber orientations at the unloaded (θ_{PPC}) and loaded configurations (θ_{exp}), respectively. The reorientations of the collagen fibers were quantified via $\theta_{reorient} = \theta_{exp} - \theta_{PPC}$, where a positive $\theta_{reorient}$ indicates a counterclockwise rotation, and a negative $\theta_{reorient}$ indicates a clockwise rotation.

2.4. Application of the affine fiber kinematics theory

Evaluation of the validity of the AFK theory requires the use of two components of our experimental measurements: (i) the unloaded fiber orientation θ_{PPC} and (ii) the deformation gradient **F**. During post-processing of the acquired pSFDI information, we selected the region of interest for the AFK analysis to be within the 2×2 fiducial marker array, as the fiber kinematics would be more realistic than in the fibers near the tine insertion. The selected region of interest was further discretized into an isoparametric 100×100 grid of query points based on the isoparametric mapping concept in the context of finite element methods (Fig. 2a, Hughes (1987)). For each query point, θ_{PPC} and θ_{exp} were determined by a weighted Euclidean distance-based approach:

$$\theta_j = \frac{\sum_{k=1}^{25} w_k \theta_k}{\sum_{k=1}^{25} w_k}, \tag{3}$$

where θ_j represents the fiber angle of the j^{th} query point, θ_k denotes the fiber angle at the k^{th} pixel within the domain of influence associated with the j^{th} query point, and w_k represents the weight, calculated as the Euclidean distance from the pixel location (p, q) of the j^{th} query point: $w_k = \sqrt{(p - p_k)^2 + (q - q_k)^2}$. Then, the unloaded fiber direction vector was constructed as $\mathbf{N}_j = [\cos(\theta_{PPC,j}), \sin(\theta_{PPC,j})]^T$ for the j^{th} query point in the selected region of interest. Interested readers are referred to Belytschko et al. (1994).

For the deformation gradient **F**, the calculations were made based on the deformation of the fiducial marker array, as tracked via a custom MATLAB program (MathWorks, MA,

USA, Fig. 2b; Sacks (2000); Billiar and Sacks (1997)). The pixel locations of the markers in the undeformed, reference (Ω_{PPC}) configurations and the deformed configurations (Ω_t) were mapped to a parametric domain, and **F** was constructed as:

$$\mathbf{F} = \begin{bmatrix} \frac{\partial x}{\partial X} & \frac{\partial x}{\partial Y} \\ \frac{\partial y}{\partial X} & \frac{\partial y}{\partial Y} \end{bmatrix} = \begin{bmatrix} \lambda_1 & \kappa_1 \\ \kappa_2 & \lambda_2 \end{bmatrix}, \tag{4}$$

where X and Y represent the undeformed marker locations, x and y denote the deformed marker locations, λ_1 and λ_2 are the axial stretches in the X- and Y-directions (i.e., Circ and Rad, respectively), and κ_j represents the shear deformations in the $X-Y$ or $Y-X$ directions.

Next, the AFK theory was adopted to determine the fiber orientation at each of the applied biaxial loading states:

$$\mathbf{n}_j = \frac{\mathbf{F} \cdot \mathbf{N}_j}{|\mathbf{F} \cdot \mathbf{N}_j|}, \tag{5}$$

where $\mathbf{n}_j = [\cos(\theta_{pred,j})\sin(\theta_{pred,j})]$ is the deformed fiber orientation associated with the j^{th} query point (Fig. 2c). To determine the AFK prediction errors, the difference between θ_{pred} and θ_{exp} was calculated as $\theta_{error} = \theta_{pred} - \theta_{exp}$, where a negative θ_{error} corresponds to an *underprediction* of the AFK theory, and a positive θ_{error} demonstrates an *overprediction*.

2.5. Statistical analysis

θ_{pred} and θ_{exp} from the 100×100 *query points* for each of the TV leaflet specimens are reported as the median±interquartile range (IQR). Quantities for all the specimens, including θ_{error} and λ, are reported as the mean±standard error of the mean (SEM). To gain insight into the correlation between any two metrics, a Pearson correlation coefficient (r) was computed ($r = 1$ indicating a positive linear correlation between the two compared metrics, $r = -1$ signifying a negative linear correlation, and $r = 0$ representing no linear correlation).

3. Results

3.1. Biaxial mechanical properties of the tricuspid valve leaflets

From the biaxial testing of the three TV leaflets, we observed the typical nonlinear, anisotropic nature of the soft tissues (Jett et al., 2018; Meador et al., 2020; Khoiy and Amini, 2016; Pokutta-Paskaleva et al., 2019). Stress-stretch curves for the TVAL, TVPL, and TVSL specimens as representative of the behavior of all the datasets are shown in Figure 3a–c. The average PPC and peak stretches for the five loading scenarios are shown in Table 1, whereas the stretches of each indiviual tested specimen are shown in Table S1. For all the tested specimens, the PPC stretches were: TVAL, $\lambda_{PPC,Circ} = 1.17 \pm 0.03$, $\lambda_{PPC,Rad} = 1.31 \pm 0.05$; TVPL, $\lambda_{PPC,Circ} = 1.17 \pm 0.03$, $\lambda_{PPC,Rad} = 1.36 \pm 0.04$,

and TVSL, $\lambda_{PPC,\,Circ} = 1.17 \pm 0.03$, $\lambda_{PPC,\,Rad} = 1.32 \pm 0.04$. Under equibiaxial tensions, the tissue stretches were found as: *Circumferential*: 1.31±0.04 (TVAL), 1.38±0.07 (TVPL), 1.49±0.07 (TVSL); *Radial*: 1.48±0.06 (TVAL), 1.62±0.07 (TVPL), 1.72±0.08 (TVSL). We also observed the TVPL to be the most anisotropic among the three TV leaflets, which was quantified by the anisotropic index = $\lambda_{Rad}/\lambda_{Circ}$: TVAL, 1.13±0.04; TVPL, 1.21±0.07; and TVSL, 1.16±0.05.

3.2. Experimentally measured collagen fiber architectures

The pSFDI-quantified CFA results for the TVAL, TVPL, and TVSL specimens as representative of the behavior of all the datasets are shown in Figure 3. The measured CFA results of all three TV leaflets under the applied *equibiaxial loading* are presented in Table 2, while the findings from the applied *non-equibiaxial loading* protocols are given in Tables S2–S4 of the Supplementary Material section. Generally, an increase in the fiber alignment was observed with increased loading, as exemplified by the DOA; however, there were less drastic changes in the fiber orientation. Specifically, the changes in the fiber orientations between the PPC and the applied equibiaxial loading states were found as: TVAL, −2.3°±2.7°; TVPL, 4.4°±3.4°; and TVSL, 1.5°±2.8°. In the applied non-equibiaxial loading, we observed more fiber reorientations towards the dominant loading direction (e.g., more circumferential fiber orientations under $T_{Circ}:T_{Rad} = 1:0.33$), with greater reorientations occurring with more disproportionate loading in the two directions (e.g., 17.8°±4.0° changes under $T_{Circ}:T_{Rad} = 0.33:1$ vs. 5.4°±2.3° changes under $T_{Circ}:T_{Rad} = 0.66:1$).

3.3. Evaluation of the AFK predictivity

The vector plots of the experimentally measured and the AFK-predicted fiber orientations for the representative TVAL, TVPL, and TVSL specimens are shown in Figures 4–6. Comparing the AFK-predicted and the experimental fiber reorientations in the TV leaflets, we observed that the AFK theory generally underpredicted the fiber rotations (Table 2). Specifically, θ_{error} from the applied equibiaxial loading protocol: TVAL, −1.6°±1.6°; TVPL, −2.9°±2.4°; and TVSL, −4.6°±1.0°. We also noted a greater disparity between the AFK theory and the pSFDI-quantified CFA under the applied non-equibiaxial loading (Tables S1–S3). For example, under $T_{Circ}:T_{Rad} = 0.33:1$, θ_{error} was found as: −4.0°±4.8° (TVAL); −5.0° ±4.3° (TVPL), and; −7.4°±4.0° (TVSL).

4. Discussion

4.1. Differences in experimental and predicted collagen fiber reorientations

In this study, we have evaluated the AFK theory for the TV leaflets *for the first time* using a biaxial testing-pSFDI approach. We observed that the AFK theory generally underpredicted the rotations of the fibers. To elaborate, weak-to-moderate negative correlations were found between $\theta_{reorient}$ and θ_{error} across all the applied loading scenarios: equibiaxial loading, $r = -0.36$; circumferentially dominant loading, $r = -0.29$ to 0.07; and radially dominant loading, $r = -0.29$ to −0.24. By comparing θ_{error} and λ, we found weak negative correlations under the applied equibiaxial loading (Circumferential, $r = -0.17$; Radial, $r = -0.02$), while under non-equibiaixal loading the correlation was stronger in the dominant loading

direction: circumferentially dominant loading, circumferential direction: $r = -0.27$ to -0.18; and radially dominant loading, radial direction: $r = -0.02$ to -0.32. The observed trends suggest that increasing collagen fiber reorientations result in an increased magnitude of underpredictions by the AFK theory, which may be further related to the increasing magnitude of the tissue deformations. This trend can be corroborated with a previous vasculature testing study that reported the AFK errors could be associated with excessive tissue deformations (Cavinato et al., 2020).

Another explanation for the mispredictions could be related to the direction of applied loading with respect to the preferred fiber orientations. A study by Lake et al. (2012a) performed uniaxial testing of human supraspinatus tendons and observed that the AFK predictions were less accurate when the loading was applied transverse to the preferred fiber orientation, and when there was a greater dispersion of fibers. We are unable to demonstrate this finding, however, because: (i) in the present study, we performed biaxial testing, and (ii) our pSFDI device quantifies the *optical anisotropy* of the material, which is not a direct measurement of the fiber dispersion. This imaging modality requires more research to be able to quantify the *structural* fiber dispersion. Regardless, it is worth highlighting that we observed a weak correlation between tissue anisotropy, which may be related to the fiber dispersion and $\theta_{error}(r = 0.15)$. Other causes for the AFK mispredictions include the potential for heterogeneous, locally varying affine kinematics (Krasny et al., 2017), the experimental testing conditions inducing varying affine or non-affine fiber kinematics (Jayyosi et al., 2017), or the fiber crimp causing significant AFK prediction errors (Lee et al., 2015).

Mispredictions from the AFK theory could also be related to the coupling between the fibers and the nonfibrous matrix. This idea is supported by a fiber-matrix model from Zhang et al. (2013), in which a more compliant non-fibrous matrix resulted in more fiber reorientations, while a stiffer nonfibrous matrix lead to more fiber stretching. This coupling effect was also observed in the modeling of collagenous gels (Lake et al., 2012b). The refinement of the AFK assumption based on these intricate non-fibrous matrix interactions requires further experimental and modeling efforts.

4.2. Considerations for constitutive modeling using affine fiber kinematics

While the exact sources of the errors from the AFK theory are uncertain, the mispredictions should be considered in the formulation of constitutive models. To this end, previous researchers have proposed various improvements to the AFK theory. For example, in the work by Lee et al. (2015) performing biaxial testing and small-angle X-ray scattering of two mitral valve leaflets, they observed that including fiber crimp in the AFK theory yielded a more accurate prediction of the fiber reorientations. This correction may not hold for the TV leaflets, however, due to the mechanical and functional differences between the atrioventricular heart valves that could cause a different microstructure, morphology, and CFA (e.g., fibrillar density and dispersion) between the two AHVs. To date, no comprehensive investigation of the TV leaflet microstructure has been performed to confirm this theory, with only one recent study making a qualitative assessment via second harmonic generation (Pokutta-Paskaleva et al., 2019). Another AFK theory adjustment was made for the experiments and modeling of gelatin co-gels by including a correction factor to

accommodate the AFK errors (Liu et al., 2017). The correction factor implementation may be more robust for imaging modalities that cannot quantify fiber crimp, such as the pSFDI method used in the present study.

While a refinement of the AFK theory could provide a more computationally efficient methodology for modeling the collagen fiber behaviors, the incorporation of the non-AFK behaviors could lead to more accurate cardiac simulations and fiber kinematics predictions. In recent literature, there has been increasing focus on modeling non-AFK, and more work should be performed to realize more accurate and computationally inexpensive models, especially for use in modeling the tissue viscoelasticity (Bianchi et al., 2020; Dhume and Barocas, 2019; Liu et al., 2017; Morin et al., 2018; Chandran and Barocas, 2006). Furthermore, experimental works should be performed to understand the non-AFK (e.g., fiber uncrimping together with fiber elongation), such as through small-angle X-ray scattering combined with biaxial mechanical testing or stress-relaxation testing.

4.3. Limitations and future extensions

There are a few limitations of the present work. First, we used the pSFDI modality to determine the CFA of the TV leaflets, and, while the pSFDI modality has been shown to provide accurate quantifications of the collagen fiber orientations (Goth et al., 2016; Jett et al., 2020; Ross et al., 2020), there is the potential for mispredictions caused by surface imperfections on the tissue (glue, dust, etc.), or glare in the polarizer. Future studies are warranted to corroborate our results with additional imaging modalities, such as small-angle scattering or multiphoton microscopy. Second, the presented CFA results depict the average collagen fiber orientation through the thickness of the tissue and there could be mispredictions caused by fiber splay. Further investigations could be made using the spatial frequency domain imaging capabilities of the system to obtain quantifications of the CFA at discrete depths of the tissue thickness, allowing for more detailed AFK-based comparisons. Investigations of the regionally varying CFA and AFK mispredictions are further necessitated by previous studies demonstrated highly heterogeneous fiber reorganizations in the aortic valve cusps (Anssari-Benam et al., 2012) Additionally, we investigated the AFK assumption for the region within the central third of the tissue using only the deformation gradient obtained from the four fiducial markers. A more refined strain field could yield more accurate AFK results (Krasny et al., 2017); however, we could not implement a refined strain field without obstructing the view of the tissue for the pSFDI system. Finally, another future study could be performed using the biaxial testing-pSFDI approach to investigate the collagen fiber reorientations in the leaflets during viscoelastic characterizations, as was observed for the aortic valve cusps (Anssari-Benam et al., 2019).

4.4. Conclusion

In this work, we have utilized the pSFDI technique to provide a detailed characterization of the load-dependent changes in the CFA of the three TV leaflets, and compared the experimentally measured fiber orientations to the AFK theory. To our knowledge, this work is *the first of its kind* for evaluating the AFK theory for the TV leaflets, which provides valuable insight for future computational modeling works that rely on AFK-based constitutive forms to describe the leaflet mechanical and microstructural behaviors.

Furthermore, another key contribution of this study is the use of biaxial testing to evaluate the AFK assumption, which is limited in the previous literature. The results of this study demonstrate the need for future experimental work to quantify the fibrous-nonfibrous matrix coupling or the non-AFK, such as crimping and uncrimping. Through an improved understanding of the collagen fiber kinematics in the TV leaflets, computational simulations can be refined for use in research areas such as tissue growth and remodeling to understand how diseases affect the CFA, which in turn impacts tissue mechanics and organ-level valve function.

Supplementary Material

Refer to Web version on PubMed Central for supplementary material.

Acknowledgments.

Funding supports from the American Heart Association Scientist Development Grant (16SDG27760143), the Presbyterian Health Foundation Team Science Grant, and, the IBEST-OUHSC Funding for Interdisciplinary Research at OU are gratefully acknowledged. CJR was supported in part by the National Science Foundation Graduate Research Fellowship (GRF 2020307284). We also acknowledge undergraduate students Grace Duginski, Hunter Lau, and Katherine Casey for their assistance in conducting the biaxial mechanical testing and pSFDI-based collage microstructural quantification

References

Anssari-Benam A, Bucchi A, 2018. Modeling the deformation of the elastin network in the aortic valve. Journal of Biomechanical Engineering 140, 011004. doi:10.1115/1.4037916.

Anssari-Benam A, Gupta H, Screen H, 2012. Strain transfer through the aortic valve. Journal of Biomechanical Engineering 134. doi:10.1115/1.4006812.

Anssari-Benam A, Screen H, Bucchi A, 2019. Insights into the micromechanics of stress-relaxation and creep behaviours in the aortic valve. Journal of the Mechanical Behavior of Biomedical Materials 93, 230–245. doi:10.1016/j.jmbbm.2019.02.011. [PubMed: 30844614]

Belytschko T, Lu YY, Gu L, 1994. Element-free galerkin methods. International Journal for Numerical Methods in Engineering 37, 229–256. doi:10.1002/nme.1620370205.

Bianchi D, Morin C, Badel P, 2020. Implementing a micromechanical model into a finite element code to simulate the mechanical and microstructural response of arteries. Biomechanics and Modeling in Mechanobiology 19, 2553–2566. doi:10.1007/s10237-020-01355-y. [PubMed: 32607921]

Billiar KL, Sacks MS, 1997. A method to quantify the fiber kinematics of planar tissues under biaxial stretch. Journal of Biomechanics 30, 753–756. doi:10.1016/S0021-9290(97)00019-5. [PubMed: 9239558]

Cavinato C, Badel P, Krasny W, Avril S, Morin C, 2020. Experimental characterization of adventitial collagen fiber kinematics using second-harmonic generation imaging microscopy: Similarities and differences across arteries, species and testing conditions, in: Multi-scale Extracellular Matrix Mechanics and Mechanobiology. Springer, pp. 123–164. doi:10.1007/978-3-030-20182-1_5.

Cavinato C, Helfenstein-Didier C, Olivier T, Du Roscoat SR, Laroche N, Badel P, 2017. Biaxial loading of arterial tissues with 3D in situ observations of adventitia fibrous microstructure: A method coupling multi-photon confocal microscopy and bulge inflation test. Journal of the Mechanical Behavior of Biomedical Materials 74, 488–498. doi:10.1016/j.jmbbm.2017.07.022. [PubMed: 28751194]

Chandran PL, Barocas VH, 2006. Affine versus non-affine fibril kinematics in collagen network: Theoretical studies of network behavior. Journal of Biomechanical Engineering 128, 259–270. doi:10.1115/1.2165699. [PubMed: 16524339]

Dhume RY, Barocas VH, 2019. Emergent structure-dependent relaxation spectra in viscoelastic fiber networks in extension. Acta Biomaterialia 87, 245–255. doi:10.1016/j.actbio.2019.01.027. [PubMed: 30682422]

Duginski GA, Ross CJ, Laurence DW, Johns CH, Lee C-H, 2020. An investigation of the effect of freezing storage on the biaxial mechanical properties of excised porcine tricuspid valve anterior leaflets. Journal of the Mechanical Behavior of Biomedical Materials 101, 103438. doi:10.1016/j.jmbbm.2019.103438. [PubMed: 31542570]

Fan R, Sacks MS, 2014. Simulation of planar soft tissues using a structural constitutive model: Finite element implementation and validation. Journal of Biomechanics 47, 2043–2054. doi:10.1016/j.jbiomech.2014.03.014. [PubMed: 24746842]

Gilbert TW, Sacks MS, Grashow JS, Woo SL-Y, Badylak SF, Chancellor MB, 2006. Fiber kinematics of small intestinal submucosa under biaxial and uniaxial stretch. Journal of Biomechanical Engineering 128, 890–898. doi:10.1115/1.2354200. [PubMed: 17154691]

Goth W, Yang B, Lesicko J, Allen A, Sacks MS, Tunnell JW, 2016. Polarized spatial frequency domain imaging of heart valve fiber structure, in: Proceedings of SPIE Volume 9710, Optical Elastography and Tissue Biomechanics III, p. 971019. doi:10.1117/12.2212812.

Hudson LT, Jett SV, Kramer KE, Laurence DW, Ross CJ, Towner RA, Baumwart R, Lim KM, Mir A, Burkhart HM, Wu Y, Lee C-H, 2020. A pilot study on linking tissue mechanics with load-dependent collagen microstructures in porcine tricuspid valve leaflets. Bioengineering 7, 60. doi:10.3390/bioengineering7020060. [PubMed: 32570939]

Hughes TJR, 1987. The Finite Element Method: Linear Static and Dynamic Finite Element Analysis. Courier Corporation.

Jacobs NT, Cortes DH, Vresilovic EJ, Elliott DM, 2013. Biaxial tension of fibrous tissue: Using finite element methods to address experimental challenges arising from boundary conditions and anisotropy. Journal of Biomechanical Engineering 135. doi:10.1115/1.4023503.

Jayyosi C, Affagard J-S, Ducourthial G, Bonod-Bidaud C, Lynch B, Bancelin S, Ruggiero F, Schanne-Klein M-C, Allain J-M, Bruyère-Garnier K, 2017. Affine kinematics in planar fibrous connective tissues: An experimental investigation. Biomechanics and Modeling in Mechanobiology 16, 1459–1473. doi:10.1007/s10237-017-0899-1. [PubMed: 28357604]

Jett SV, Hudson LT, Baumwart R, Bohnstedt BN, Mir A, Burkhart HM, Holzapfel GA, Wu Y, Lee C-H, 2020. Integration of polarized spatial frequency domain imaging (pSFDI) with a biaxial mechanical testing system for quantification of load-dependent collagen architecture in soft collagenous tissues. Acta Biomaterialia 102, 149–168. doi:10.1016/j.actbio.2019.11.028. [PubMed: 31734412]

Jett SV, Laurence DW, Kunkel RP, Babu AR, Kramer KE, Baumwart R, Towner RA, Wu Y, Lee C-H, 2018. An investigation of the anisotropic mechanical properties and anatomical structure of porcine atrioventricular heart valves. Journal of the Mechanical Behavior of Biomedical Materials 87, 155–171. doi:10.1016/j.jmbbm.2018.07.024. [PubMed: 30071486]

Khoiy KA, Amini R, 2016. On the biaxial mechanical response of porcine tricuspid valve leaflets. Journal of Biomechanical Engineering 138, 104504. doi:10.1115/1.4034426.

Kramer KE, Ross CJ, Laurence DW, Babu AR, Wu Y, Towner RA, Mir A, Burkhart HM, Holzapfel GA, Lee C-H, 2019. An investigation of layer-specific tissue biomechanics of porcine atrioventricular valve anterior leaflets. Acta Biomaterialia 96, 368–384. doi:10.1016/j.actbio.2019.06.049. [PubMed: 31260822]

Krasny W, Morin C, Magoariec H, Avril S, 2017. A comprehensive study of layer-specific morphological changes in the microstructure of carotid arteries under uniaxial load. Acta Biomaterialia 57, 342–351. doi:10.1016/j.actbio.2017.04.033. [PubMed: 28499632]

Kunzelman KS, Cochran RP, Murphree SS, Ring WS, Verrier ED, Eberhart RC, 1993. Differential collagen distribution in the mitral valve and its influence on biomechanical behaviour. The Journal of Heart Valve Disease 2, 236–244. [PubMed: 8261162]

Lake SP, Cortes DH, Kadlowec JA, Soslowsky LJ, Elliott DM, 2012a. Evaluation of affine fiber kinematics in human supraspinatus tendon using quantitative projection plot analysis. Biomechanics and Modeling in Mechanobiology 11, 197–205. doi:10.1007/s10237-011-0303-5. [PubMed: 21461899]

Lake SP, Hadi MF, Lai VK, Barocas VH, 2012b. Mechanics of a fiber network within a non-fibrillar matrix: Model and comparison with collagen-agarose co-gels. Annals of Biomedical Engineering 40, 2111–2121. doi:10.1007/s10439-012-0584-6. [PubMed: 22565816]

Lanir Y, 2017. Multi-scale structural modeling of soft tissues mechanics and mechanobiology. Journal of Elasticity 129, 7–48. doi:10.1007/s10659-016-9607-0.

Laurence DW, Ross CJ, Jett SV, Johns CH, Echols AL, Baumwart R, Towner RA, Liao J, Bajona P, Wu Y, Lee C-H, 2019. An investigation of regional variations in the biaxial mechanical properties and stress relaxation behaviors of porcine atrioventricular heart valve leaflets. Journal of Biomechanics 83, 16–27. doi:10.1016/j.jbiomech.2018.11.015. [PubMed: 30497683]

Lee C-H, Zhang W, Liao J, Carruthers CA, Sacks JI, Sacks MS, 2015. On the presence of affine fibril and fiber kinematics in the mitral valve anterior leaflet. Biophysical Journal 108, 2074–2087. doi:10.1016/j.bpj.2015.03.019. [PubMed: 25902446]

Liu T, Hall TJ, Barbone PE, Oberai AA, 2017. Inferring spatial variations of microstructural properties from macroscopic mechanical response. Biomechanics and Modeling in Mechanobiology 16, 479–496. doi:10.1007/s10237-016-0831-0. [PubMed: 27655420]

Meador WD, Mathur M, Sugerman GP, Jazwiec T, Malinowski M, Bersi MR, Timek TA, Rausch MK, 2020. A detailed mechanical and microstructural analysis of ovine tricuspid valve leaflets. Acta Biomaterialia 102, 100–113. doi:10.1016/j.actbio.2019.11.039. [PubMed: 31760220]

Morin C, Avril S, Hellmich C, 2018. Non-affine fiber kinematics in arterial mechanics: A continuum micromechanical investigation. Zeitschrift für Angewandte Mathematik und Mechanik 98, 2101–2121. doi:10.1002/zamm.201700360.

Pham T, Sulejmani F, Shin E, Wang D, Sun W, 2017. Quantification and comparison of the mechanical properties of four human cardiac valves. Acta Biomaterialia 54, 345–355. doi:10.1016/j.actbio.2017.03.026. [PubMed: 28336153]

Pierlot CM, Moeller AD, Lee JM, Wells SM, 2015. Biaxial creep resistance and structural remodeling of the aortic and mitral valves in pregnancy. Annals of Biomedical Engineering 43, 1772–1785. doi:10.1007/s10439-014-1230-2. [PubMed: 25564325]

Pokutta-Paskaleva A, Sulejmani F, DelRocini M, Sun W, 2019. Comparative mechanical, morphological, and microstructural characterization of porcine mitral and tricuspid leaflets and chordae tendineae. Acta Biomaterialia 85, 241–252. doi:10.1016/j.actbio.2018.12.029. [PubMed: 30579963]

Ross CJ, Hsu M-C, Baumwart R, Mir A, Burkhart HM, Holzapfel GA, Lee C-H, 2020. Quantification of load-dependent changes in the collagen fiber architecture for the strut chordae tendineae-leaflet insertion of porcine atrioventricular heart valves. Biomechanics and Modeling in Mechanobiology doi:10.1007/s10237-020-01379-4.

Ross CJ, Laurence DW, Wu Y, Lee C-H, 2019. Biaxial mechanical characterizations of atrioventricular heart valves. Journal of Visualized Experiments 146, e59170. doi:10.3791/59170.

Sacks MS, 2000. Biaxial mechanical evaluation of planar biological materials. Journal of Elasticity 61. doi:10.1023/A:1010917028671.

Sacks MS, Smith DB, Hiester ED, 1997. A small angle light scattering device for planar connective tissue microstructural analysis. Annals of Biomedical Engineering 25, 678–689. doi:10.1007/BF02684845. [PubMed: 9236980]

Sacks MS, Smith DB, Hiester ED, 1998. The aortic valve microstructure: Effects of transvalvular pressure. Journal of Biomedical Materials Research 41, 131–141. doi:10.1002/(SICI)1097-4636(199807)41:1$<$131::AID-JBM16$>$3.0.C0;2-Q. [PubMed: 9641633]

Sacks MS, Yoganathan AP, 2007. Heart valve function: A biomechanical perspective. Philosophical Transactions of the Royal Society B: Biological Sciences 362, 1369–1391. doi:10.1098/rstb.2007.2122. [PubMed: 17588873]

Tadmor EB, Miller RE, Elliott RS, 2012. Continuum Mechanics and Thermodynamics: From Fundamental Concepts to Governing Equations. Cambridge University Press.

Zhang L, Lake SP, Lai VK, Picu CR, Barocas VH, Shephard MS, 2013. A coupled fiber-matrix model demonstrates highly inhomogeneous microstructural interactions in soft tissues under tensile load. Journal of Biomechanical Engineering 135. doi:10.1115/1.4023136.

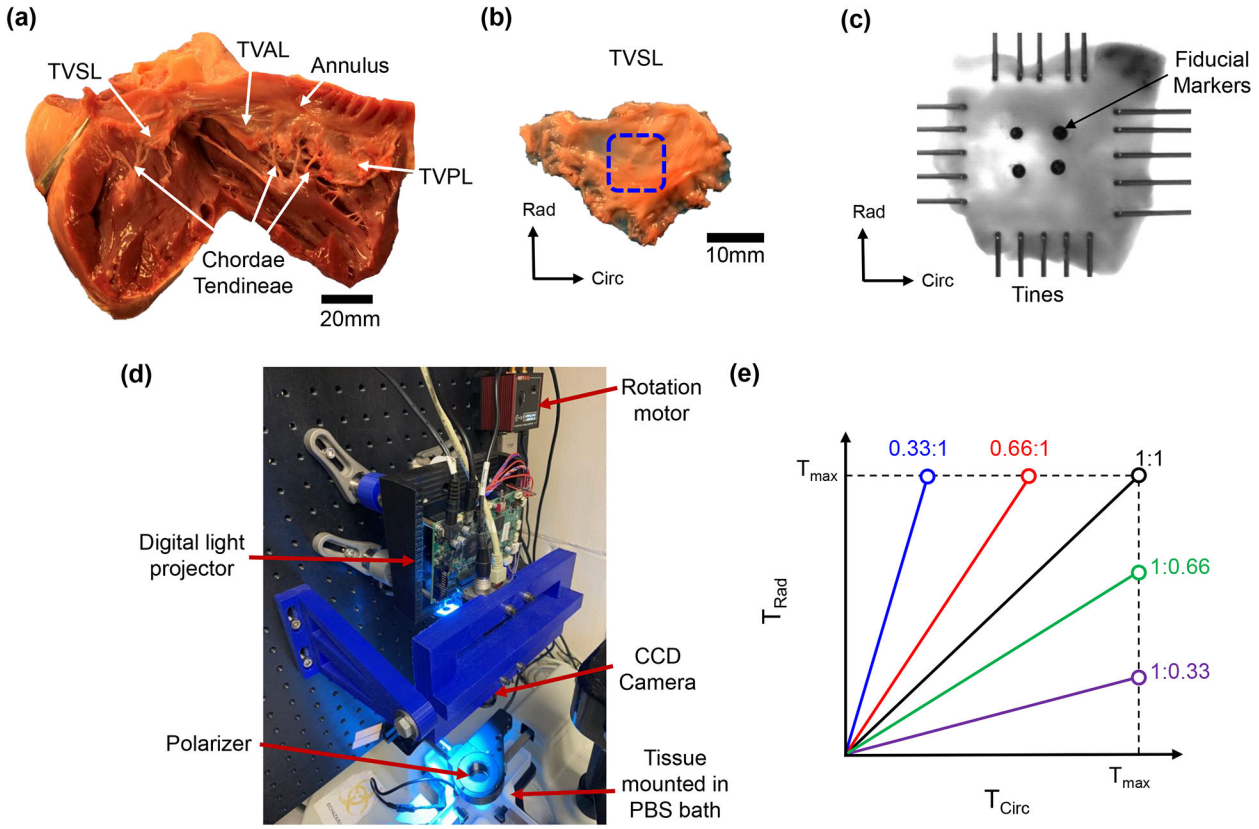

Figure 1:

(a) Porcine tricuspid valves dissected to obtain the (b) TV leaflets. A 10×10mm square specimen prepared from the central, belly region of the leaflet and (c) mounted via tined BioRakes to a (d) a coupled pSFDI-biaxial testing device. (e) Schematic of the membrane tension (T) loading ratios in the biaxial mechanical testing.

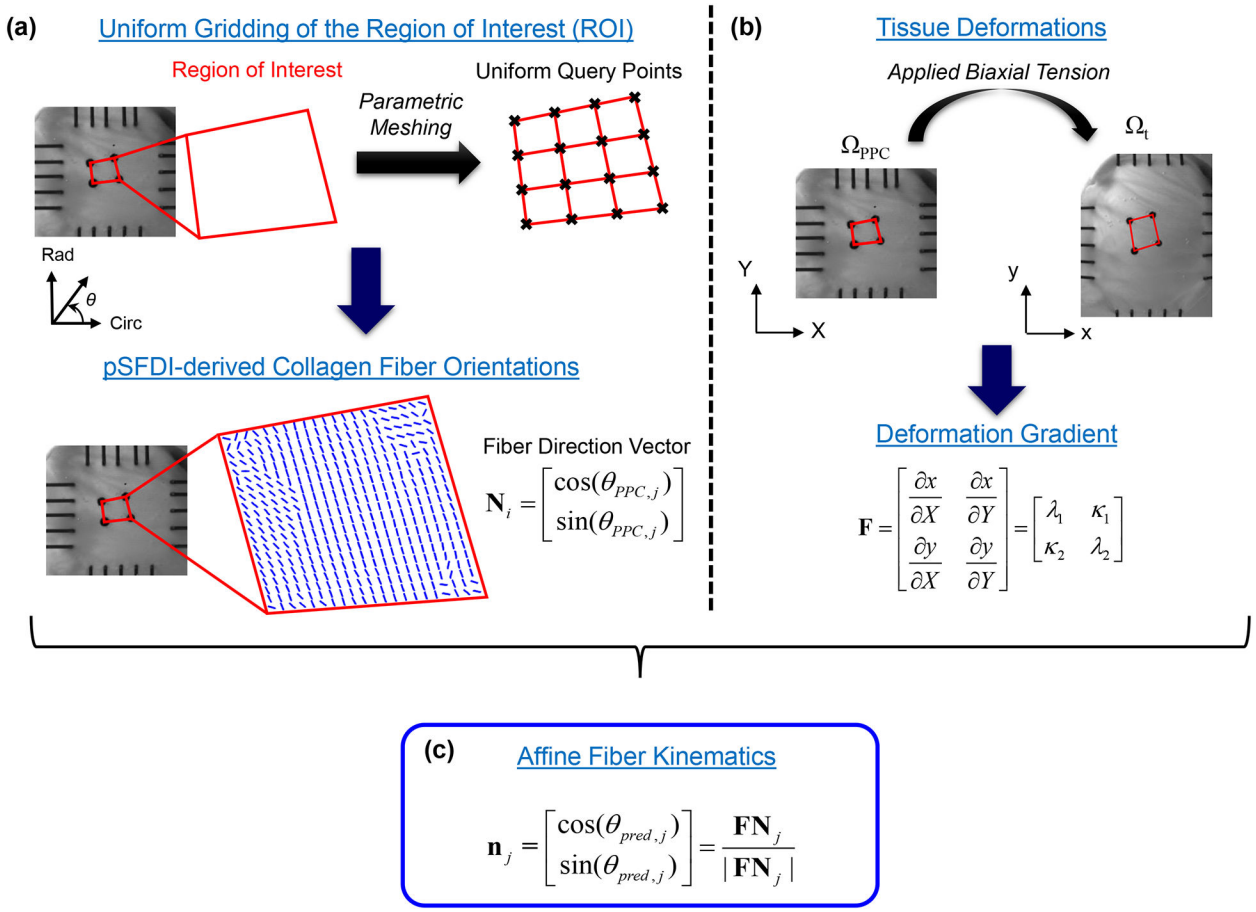

Figure 2:

A schematic diagram of the methods used to acquire (a) the pSFDI-measured collagen fiber angles and (b) the experimentally measured deformation gradient **F** from biaxial testing that were used to (c) predict the collagen fiber orientations from affine fiber kinematics theory.

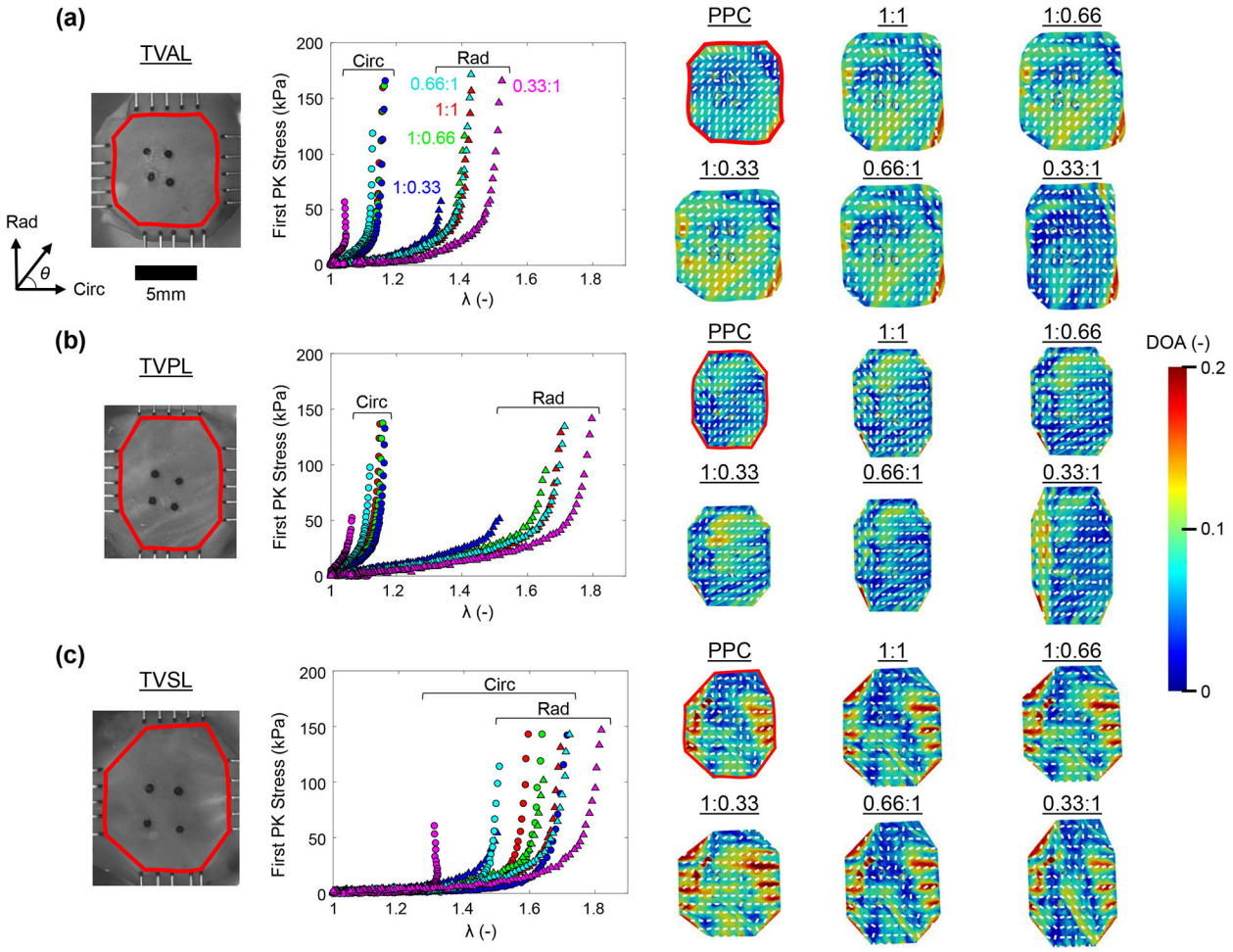

Figure 3:

Representative experimentally measured results from (a) TVAL #11, (b) TVPL #6, and (c) TVSL #10. The experimental photo from the pSFDI camera is provided (*left column*), along with the biaxial mechanical testing results (*middle column*), and the pSFDI-based collagen fiber orientations at the post-preconditioning (PPC) configuration and other applied biaxial tension protocols (*right column*). Note that the region of interest shown is for the full tissue specimen, while the AFK analysis was only performed for the region delimited by the fiducial markers.

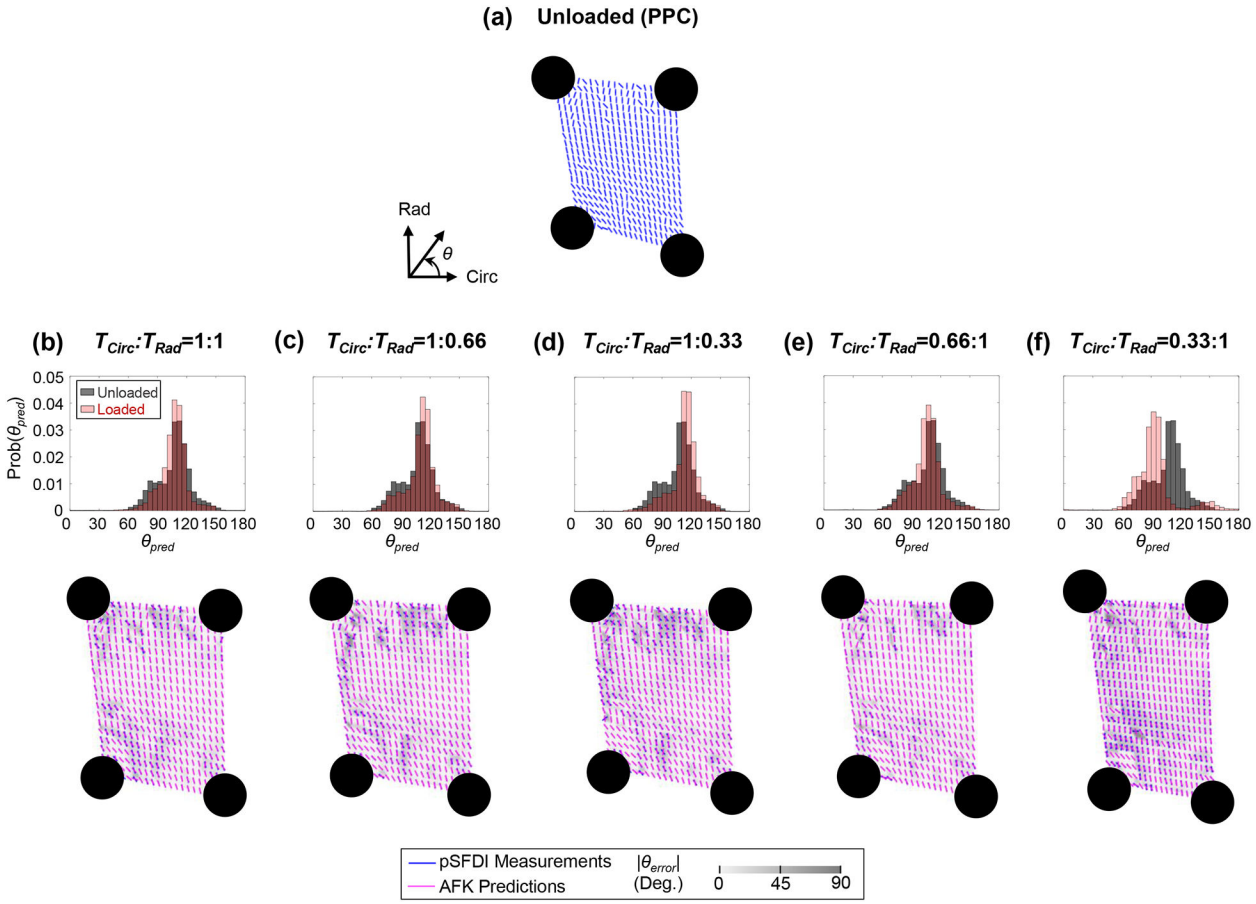

Figure 4:

Comparisons of the AFK-predicted and pSFDI-measured collagen fiber orientations for a representative TVAL specimen (TVAL #11) at the (a) PPC deformation (experimental only) and at the peak deformation of various applied biaxial loading states: (b) $T_{Circ}:T_{Rad} = 1:1$, (c) $T_{Circ}:T_{Rad} = 1:0.66$, (d) $T_{Circ}:T_{Rad} = 1:0.33$, (e) $T_{Circ}:T_{Rad} = 0.66:1$, and (f) $T_{Circ}:T_{Rad} = 0.33:1$. Dashed lines denote the predicted and experimentally measured collagen fiber orientations for some selected pixels, the grayscale gradient represents the absolute error between the predicted and experimental findings, and the black circles represent the positions of the fiducial markers. Histograms denote the probability for the experimental collagen fiber orientations at each five-degree increment.

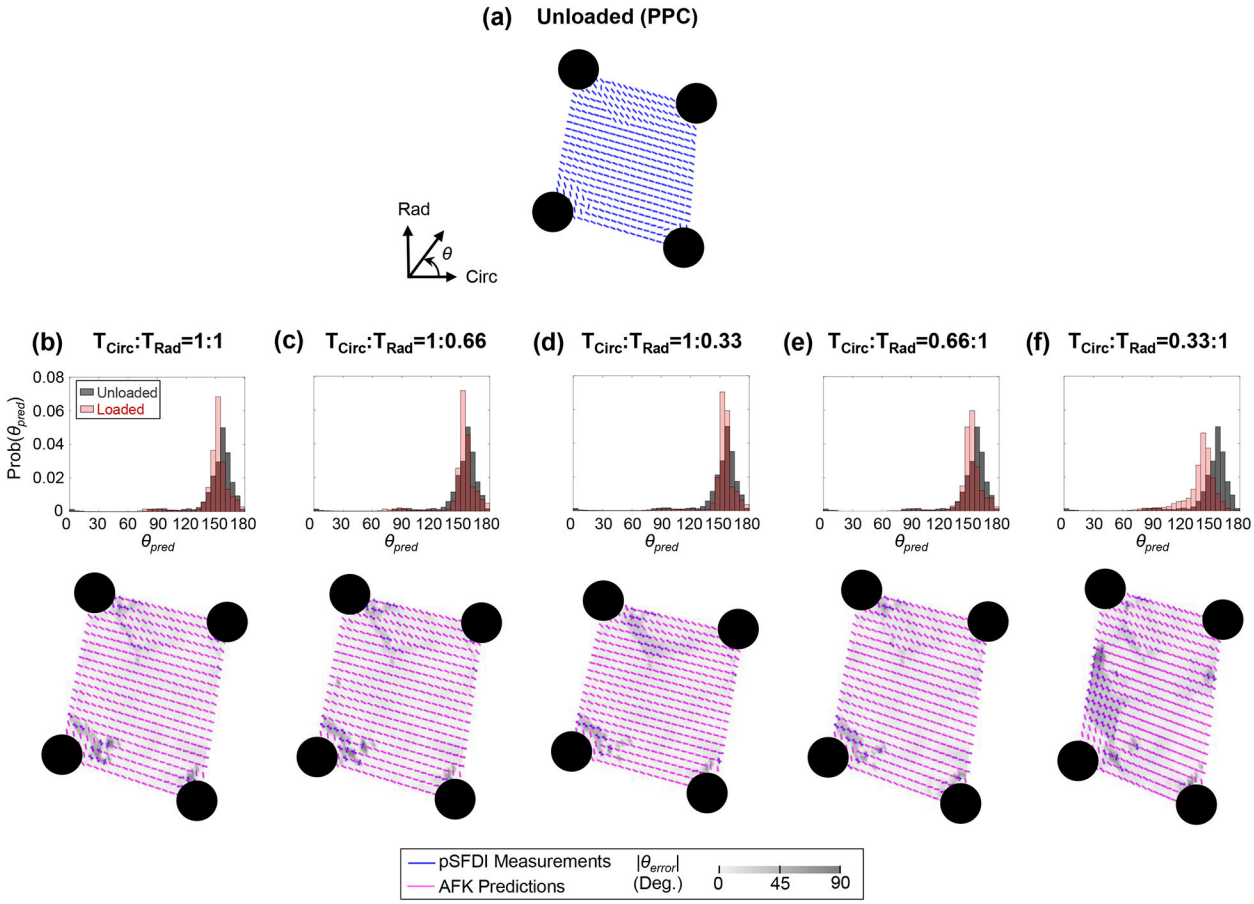

Figure 5:

Comparisons of the AFK-predicted and pSFDI-measured collagen fiber orientations for a representative TVPL specimen (TVPL #6) at the (a) PPC deformation (experimental only) and at the peak deformation of various applied biaxial loading states: (b) $T_{Circ}:T_{Rad} = 1:1$, (c) $T_{Circ}:T_{Rad} = 1:0.66$, (d) $T_{Circ}:T_{Rad} = 1:0.33$, (e) $T_{Circ}:T_{Rad} = 0.66:1$, and (f) $T_{Circ}:T_{Rad} = 0.33:1$. Dashed lines denote the predicted and experimentally measured collagen fiber orientations for some selected pixels, the grayscale gradient represents the absolute error between the predicted and experimental findings, and the black circles represent the positions of the fiducial markers. Histograms denote the probability for the experimental collagen fiber orientations at each five-degree increment.

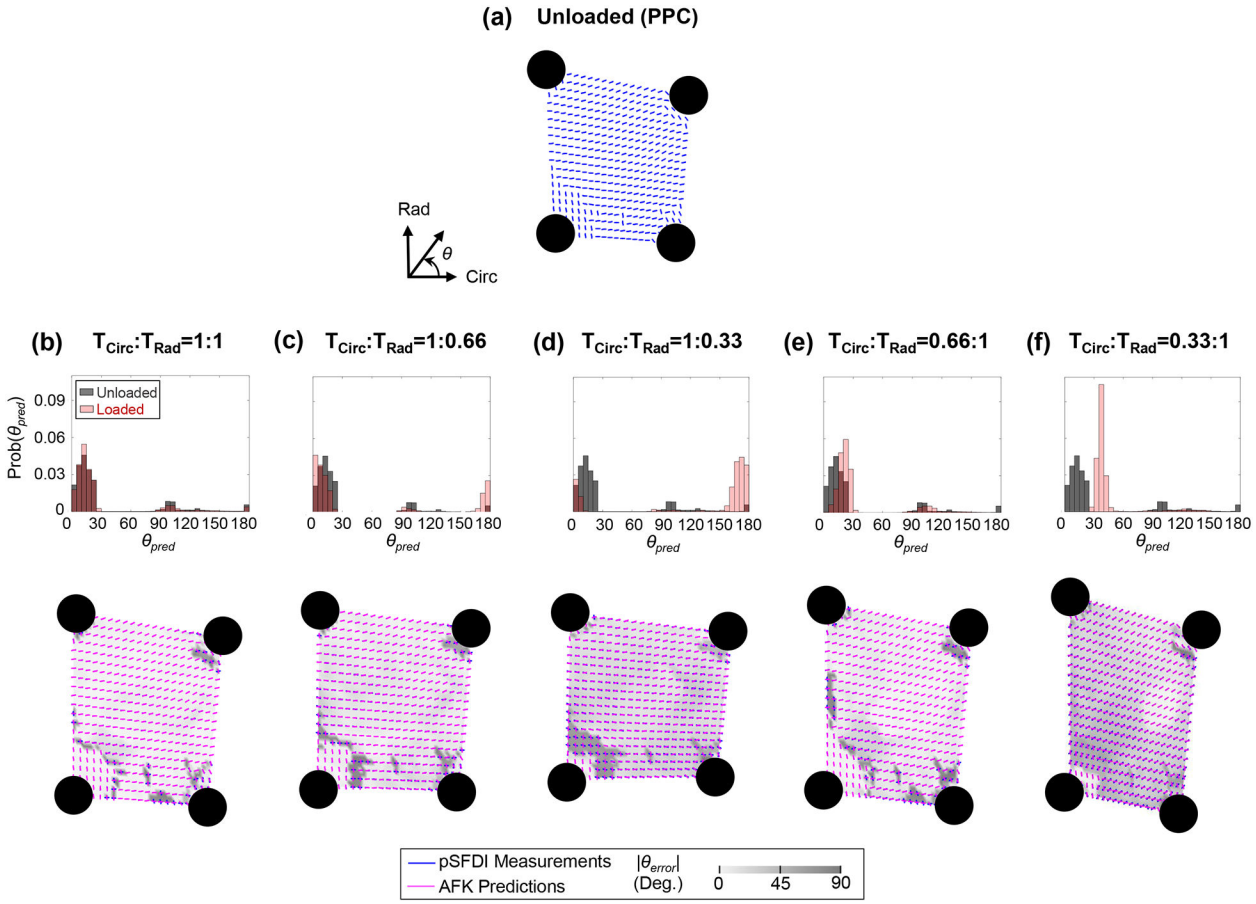

Figure 6:

Comparisons of the AFK-predicted and pSFDI-measured collagen fiber orientations for a representative TVSL specimen (TVSL #10) at the (a) PPC deformation (experimental only) and at the peak deformation of various applied biaxial loading states: (b) $T_{Circ}:T_{Rad} = 1:1$, (c) $T_{Circ}:T_{Rad} = 1:0.66$, (d) $T_{Circ}:T_{Rad} = 1:0.33$, (e) $T_{Circ}:T_{Rad} = 0.66:1$, and (f) $T_{Circ}:T_{Rad} = 0.33:1$. Dashed lines denote the predicted and experimentally measured collagen fiber orientations for some selected pixels, the grayscale gradient represents the absolute error between the predicted and experimental findings, and the black circles represent the positions of the fiducial markers. Histograms denote the probability for the experimental collagen fiber orientations at each five-degree increment.

Table 1:

The post-preconditioning (PPC) stretches and peak stretches of the TVAL, TVPL, and TVSL specimens under the five applied biaxial tensions (T_{Circ}:T_{Rad}). Results are presented as the mean±SEM.

	TVAL		TVPL		TVSL	
Loading Protocol	**Circ**	**Rad**	**Circ**	**Rad**	**Circ**	**Rad**
PPC	1.17±0.03	1.31±0.05	1.17±0.03	1.36±0.04	1.17±0.03	1.32±0.04
1:1	1.31±0.04	1.48±0.06	1.38±0.07	1.62±0.07	1.49±0.07	1.72±0.08
1:0.66	1.33±0.05	1.44±0.06	1.40±0.08	1.57±0.07	1.53±0.07	1.65±0.07
1:0.33	1.36±0.05	1.33±0.05	1.43±0.08	1.43±0.06	1.58±0.07	1.47±0.06
0.66:1	1.27±0.04	1.50±0.07	1.34±0.07	1.64±0.07	1.43±0.06	1.75±0.08
0.33:1	1.15±0.03	1.58±0.08	1.25±0.06	1.69±0.07	1.26±0.05	1.85±0.08

Table 2:

Comparisons of the collagen fiber angle between the pSFDI measurements and AFK predictions at the post-preconditioning (PPC) and peak equibiaxial deformations ($T_{Circ}:T_{Rad} = 1:1$) for all TVAL, TVPL, and TVSL specimens. The θ_{median} and IQR are provided for the 100×100 grids considered for each specimen, and the θ_{error} between the measured and predicted fiber orientations at the peak deformation are expressed as the mean±SD.

		PPC		$T_{Circ}:T_{Rad} = 1:1$				
		Measured θ_{exp}		Measured θ_{exp}		Predicted θ_{pred}		θ_{error}
Leaflet	Specimen ID	Median	IQR	Median	IQR	Median	IQR	
TVAL	1	149.1°	10.9°	154.4°	7.6°	141.2°	8.7°	−12.6°±22.9°
	2	115.4°	39.5°	142.5°	45.2°	116.3°	39.9°	−4.5°±21.2°
	3	38.4°	21.5°	40.9°	11.0°	38.0°	19.3°	−6.9°±23.8°
	4	162.6°	24.4°	156.7°	62.9°	162.1°	17.2°	−1.8°±28.2°
	5	96.5°	13.5°	92.2°	9.5°	99.8°	14.7°	−0.3°±12.6°
	6	111.2°	11.4°	114.3°	10.5°	113.4°	11.2°	0.4°±7.8°
	7	80.8°	6.6°	78.2°	5.7°	82.8°	7.4°	−1.2°±20.8°
	8	151.5°	3.5°	146.5°	4.1°	150.5°	3.7°	5.0°±12.2°
	9	141.1°	43.1°	144.5°	30.3°	141.5°	43.6°	5.5°±25.5°
	10	132.4°	13.5°	134.6°	15.3°	129.7°	13.6°	−4.0°±7.5°
	11	104.9°	14.7°	104.7°	8.6°	103.1°	15.1°	2.4°±13.5°
TVPL	1	112.6°	10.0°	118.4°	14.7°	115.2°	10.4°	−1.7°±16.8°
	2	16.8°	144.8°	21.2°	137.3°	19.4°	138.0°	0.1°±20.1°
	3	157.8°	9.9°	155.8°	9.7°	154.3°	10.3°	−2.2°±13.6°
	4	124.4°	21.3°	121.8°	21.0°	123.5°	20.7°	2.0°±22.6°
	5	136.0°	11.1°	94.6°	77.3°	134.3°	11.7°	−30.8°±38.9°
	6	156.6°	13.3°	152.2°	8.2°	155.4°	14.2°	0.0°±14.9°
	7	152.2°	15.0°	155.5°	17.6°	152.3°	15.0°	−3.3°±20.2°
	8	169.6°	14.1°	162.2°	15.4°	166.0°	78.3°	10.0°±20.6°
	9	121.8°	24.8°	119.6°	26.5°	119.7°	20.8°	−6.0°±14.6°
	10	132.8°	31.0°	136.9°	34.7°	128.9°	28.6°	−6.7°±13.6°
	11	80.1°	26.0°	57.9°	41.1°	81.9°	25.6°	−1.0°±−0.9°
	12	136.7°	24.9°	142.5°	28.1°	136.5°	25.4°	−0.9°±20.2°
	13	78.5°	11.7°	79.9°	13.6°	76.5°	12.1°	−2.9°±12.5°
	14	73.5°	32.0°	68.6°	36.5°	75.1°	30.1°	2.7°±14.1°
TVSL	1	113.1°	23.9°	123.8°	32.4°	114.7°	22.6°	−4.9°±21.1°
	2	147.1°	21.0°	139.0°	64.0°	145.9°	21.3°	−4.2°±19.6°
	3	165.6°	20.6°	148.6°	155.3°	164.8°	23.6°	−6.9°±29.0°
	4	8.7°	99.3°	10.2°	7.5°	9.6°	94.1°	−12.2°±29.7°
	5	101.4°	37.8°	108.3°	33.8°	98.1°	39.5°	−4.8°±15.3°
	6	102.5°	27.3°	100.4°	35.3°	101.7°	24.9°	−8.9°±29.5°

		PPC		$T_{Circ}:T_{Rad}=1:1$				
		Measured θ_{exp}		Measured θ_{exp}		Predicted θ_{pred}		θ_{error}
Leaflet	**Specimen ID**	**Median**	**IQR**	**Median**	**IQR**	**Median**	**IQR**	
	7	124.5°	49.4°	102.1°	74.8°	126.8°	40.7°	−4.4°±38.8°
	8	34.1°	130.8°	35.6°	128.7°	36.0°	128.0°	−1.6°±24.0°
	9	106.5°	16.9°	108.2°	17.2°	106.2°	15.8°	−1.4°±12.6°
	10	15.2°	14.5°	14.2°	14.0°	16.4°	14.7°	−1.0°±19.7°
	11	92.4°	13.9°	96.8°	70.6°	90.3°	13.3°	−2.5°±47.0°
	12	156.8°	20.5°	162.7°	13.6°	153.9°	20.6°	−2.8°±32.9°